

# **Reverberation Mapping Analysis of the 2016 HST Campaign on NGC 4593**

Lukas Diehl

George-August-Universität Göttingen

November 6, 2025

## **Abstract**

Abstract

# Contents

<b>1</b>	<b>Introduction</b>	<b>4</b>
<b>2</b>	<b>Scientific Background</b>	<b>5</b>
2.1	Active Galactic Nuclei . . . . .	5
2.1.1	Structure and Spectral Features of an AGN . . . . .	6
2.1.2	Classification . . . . .	8
2.1.3	Unification Model . . . . .	10
2.1.4	Variability . . . . .	12
2.2	Reverberation Mapping . . . . .	12
2.2.1	Principle . . . . .	13
2.2.2	Cross-Correlation Function and Lag Measurement . . . . .	13
2.2.3	Black-Hole Mass . . . . .	14
2.3	Bowen Fluorescence . . . . .	15
<b>3</b>	<b>Campaign and Analysis</b>	<b>16</b>
3.1	NGC4593 . . . . .	16
3.2	2016 Campaign by E. M. Cackett . . . . .	17
3.3	Intercalibration and Determination of AVG and RMS Spectra . . . . .	18
<b>4</b>	<b>Reverberation Mapping Analysis of NGC4593</b>	<b>20</b>
4.1	Line Determination . . . . .	20
4.2	Emission Line and Continua Measurement . . . . .	22
4.3	Lightcurves . . . . .	24
4.3.1	Continua . . . . .	24
4.3.2	Emission Lines . . . . .	25
4.4	Line Profiles . . . . .	25
4.5	Time Lag and BH Masses . . . . .	25
<b>5</b>	<b>Discussion</b>	<b>32</b>

# List of Figures

2.1	Different components of an AGN. Adapted from (Mo, Bosch, and White 2010) Figure 14.3. . . . .	5
2.2	An example of Seyfert I and Seyfert II spectra illustrating their differences. Broad lines, such as the highlighted $H\alpha$ and $H\beta$ , are only present in the Seyfert I spectrum, whereas forbidden [O III] lines are visible in both cases. Adopted from (Runco 2015). . . . .	9
2.3	This graphic shows a schematic of the unification model of an AGN. The figure was adopted from (Beckmann and Shrader 2013). . . . .	11
3.1	A DSS image of NGC4593. . . . .	17
3.2	Comparison of the optical spectral range from the 2016 campaign of NGC 4593, showing the effects of [O III] $\lambda 5007$ intercalibration on both the individual spectra (top) and the derived average and rms spectra (bottom). . . . .	19
4.1	Optical AVG and RMS spectrum with determined emission lines. . .	20
4.2	UV spectrum AVG and RMS spectrum with determined emission lines	21
4.3	.....	26
4.4	AVG RMS Spektrum . . . . .	27
4.5	AVG RMS Spektrum . . . . .	28
4.6	AVG RMS Spektrum . . . . .	29
4.7	AVG RMS Spektrum . . . . .	30
4.8	AVG RMS Spektrum . . . . .	31

# List of Tables

3.1	Overview of STIS Grating Characteristics (Space Telescope Science Institute 2025) . . . . .	17
4.1	Integration Limits and Pseudo-Continua of the measured emission lines . . . . .	23
4.2	Integration Limits of the measured continua . . . . .	23
4.3	Variability statistics of the investigated continua and broad lines with minimum (2) and maximum flux density or integrated flux (3), peak-to-peak ratio (4), mean (5), standard deviation (6) and fractional variation (7). . . . .	24

# 1. Introduction

The barred spiral Galaxy NGC 4593 belongs to the active galaxies with an active galactic nucleus (AGN). Its among some of the most luminous objects in the universe emitting radiation across the entire electromagnetic spectrum. Most of the radiation originates from the AGN itself, outshining its host-galaxy by multiple orders of magnitude. In contrast to inactive galaxies, such as the milky-way, the supermassive black-hole (SMBH) in an active galaxies is still absorbing matter from the central region, creating thermal radiation as well as other non-thermal processes like photo-ionization and followed recombination. While the central AGN region is not directly resolvable, measuring and analyzing the spectral features in its emissions makes it possible to study its structure. If an AGN is variable, which is the case for NGC4593, it is possible to measure time lags between the light-curves of different spectral features in the spectra. With these time lags and the measurable widths of the emission lines in the spectra, it is possible to determine the radii of the different emitting regions around the SMBH. This kind of analysis is called reverberation mapping (RM) and can be further used to estimate the mass of the SMBH.

To execute a reverberation mapping analysis an observation campaign over multiple days or weeks is needed, to measure the variability of NGC4593. For that, an observation campaign from the Hubble Space Telescope (HST) was used, which was conducted by E. M. Cackett (Edward M Cackett et al. 2018).

Based on this campaign, this thesis will cover a classical reverberation mapping analysis of NGC4593, with a particular focus on spectral features like the optical broad emission lines such as the Balmer emission lines. An additional focus will be on the variability and time lag of the OI  $\lambda 8446$  emission line and a possible Bowen-fluorescence process driven by the Lyman emission lines.

## 2. Scientific Background

### 2.1 Active Galactic Nuclei

Active Galactic Nuclei (AGN) refers to the central region of active Galaxies. Those objects are among the most luminous objects in the universe, with bolometric luminosities ranging from  $10^{41}$  to  $10^{48}$  erg s $^{-1}$ , outshining entire galaxies by several orders of magnitude (Bradley M. Peterson 1997). First explanation tries were unusually dense star clusters or repeated supernova explosions as power sources, but these models soon proved insufficient to account for the observed luminosities, which spans over the entire electromagnetic spectrum. Today it is understood, that these enormous luminosities are powered by accretion of matter onto a supermassive black hole (SMBH) in the center of the AGN. The most common model for this accretion is a hot, rotating accretion disk around the SMBH, which is responsible for most of the observed radiation (Shakura and Sunyaev 1973).

The following sections will outline the key components of an AGN, introduce the unification model that connects various AGN types, and summarize common classification schemes. A special focus will be on AGN variability, which plays a central role in the reverberation mapping analysis conducted in this thesis.

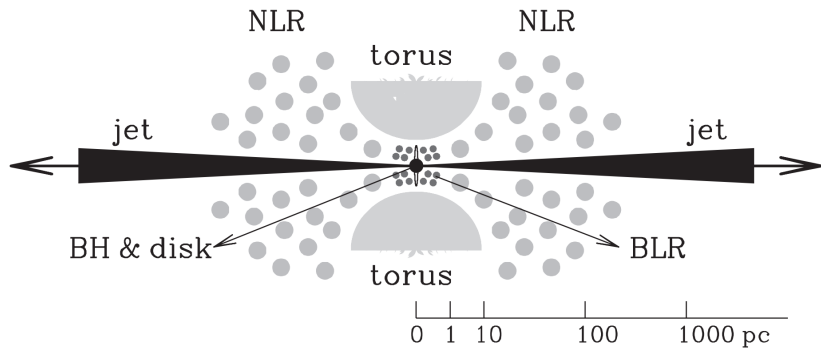


Figure 2.1: Different components of an AGN. Adapted from (Mo, Bosch, and White 2010) Figure 14.3.

### 2.1.1 Structure and Spectral Features of an AGN

Figure 2.1 illustrates a schematic structure of an AGN, which can be distributed in multiple components: a central supermassive black hole (SMBH), an accretion disk that feeds the SMBH, a surrounding dusty torus, and ionized gas regions known as the broad-line region (BLR) and narrow-line region (NLR). Additionally the figure shows relativistic jets that launch perpendicular to the accretion disk plain, which will not be further discussed in this section, due to lack of relevance for this thesis.

#### Supermassive Black Hole and Accretion Disk

The center of an AGN is formed by a supermassive black hole (SMBH), with typical masses between  $10^6 M_\odot$  and  $10^{10} M_\odot$ . It does not contribute to the AGN spectrum by itself, but acts as the central engine for all observed spectral features of the AGN. It dominates the gravitational potential and other than inactive Galaxies, like the milky-way, it is surrounded by an accretion disk. Due to viscosity processes within the disk, like turbulent friction or magneto-rotational instability, the angular momentum of the matter is getting transported further out of the disk, which leads to a spiraling matter flow inwards the SMBH. The accretion disk itself is a geometrically thin and optically thick structure composed of ionized gas in differential rotation around the SMBH. The disk consists primarily of ionized hydrogen and helium, with traces of heavier elements. It extends from the innermost stable circular orbit (ISCO) near the event horizon out to distances of several light-days. The radial extent of the disk is relatively small compared to galactic scales and typical ranges from a few light-hours to a few light-days, corresponding to about  $10^{-3}$  to  $10^{-2}$  pc (Netzer 2013; Hickox and Alexander 2018; Shakura and Sunyaev 1973).

During the accretion process a significant fraction of the gravitational energy of the matter is transformed into thermal radiation, which accounts for the enormous luminosity observed in AGNs and heats the accretion disk up to very high temperatures depending on the size of the SMBH. As an example, the maximum effective temperature for an accretion disk around a SMBH with  $M = 10^8, M_\odot$  is on the order of several  $\times 10^5$  K, leading to UV and optical emission. In comparison, disks around stellar-mass black holes reach much higher temperatures (up to a few  $\times 10^6$  K), emitting mostly in X-rays. Due to the temperature gradient with hotter regions in the inner disk, the emitted spectrum can not be described as a single black-body. Instead, it results from combination of many black-body-like components at different temperatures, often referred to as a multi-color black-body. This creates a broad optical-UV continuum emitting ionized photons, which play a crucial role for

the other spectral features. They interact with the surrounding gas clouds near the nucleus, causing photo-ionization followed by recombination. This process leads to different types of strong emission lines, which are characteristic features of AGN spectra (Netzer 2013; Osterbrock 1989).

### Broad-Line and Narrow-Line Region

Geometrically above and below the accretion disk plain, lies a distribution of gas clouds, which are photo-ionized by the energetic photons of the accretion disk continuum. The innermost of these clouds is the broad-line region (BLR), located at distances of a few light-days to light-weeks from the central SMBH (see Figure 2.1). The BLR consists of dense gas clouds with electron densities of  $n_e \sim 10^9\text{--}10^{11}\text{cm}^{-3}$ , moving at high velocities of several thousand kilometers per second due to the strong gravitational influence of the SMBH. These velocities lead to a significant Doppler broadening of permitted emission lines and line widths of around  $3000\text{ km s}^{-1}$ . As described earlier, the BLR is primarily photo-ionized by the continuum radiation emitted from the accretion disk. As a result, the line emission from this region is strongly correlated with the continuum emission, which is particularly important for a reverberation mapping analysis, which will be discussed later in Section 2.2. The exact geometry of the BLR remains uncertain, with models ranging from a spherical distribution of clouds to a flattened disk-like structure. Broad emission lines appear in permitted transitions such as H $\alpha$ , H $\beta$  and Ly $\alpha$ . (Netzer 2013; Osterbrock 1989; Bradley M. Peterson 1997)

Even further out lies the narrow-line region (NLR). The gas in this region moves at much lower velocities, resulting in emission lines with widths typically below  $1000\text{ km s}^{-1}$ . In contrast to the BLR, the NLR allows both permitted and forbidden transitions. Forbidden lines, such as [O III]  $\lambda 5007$ , arise because collisional de-excitation is inefficient at the relatively low densities of the NLR ( $n_e \sim 10^2\text{--}10^6\text{cm}^{-3}$ ) (Osterbrock 1989). The narrow [O III]  $\lambda 5007$  line was used to intercalibrate the spectra of the various observations employed in this thesis (see Chapter 3).

### Dusty Torus

Surrounding the accretion disk and broad-line region is the dusty torus, a geometrically thick and optically dense structure composed of gas and dust. It extends from a radius, where dust can survive the intense radiation of the accretion disk, out to scales of a few parsecs. The torus likely has a clumpy distribution and plays a crucial role in the unified model of AGNs which will be discussed in a later section (Netzer 2013; Hickox and Alexander 2018). The dust in the torus absorbs a

significant fraction of the UV and optical radiation emitted by the accretion disk and re-emits it thermally in the infrared. As a result, AGNs typically exhibit strong infrared emission, with the peak wavelength depending on the temperature of the dust in the torus. This reprocessed radiation provides an important observational signature and can be used to trace obscured AGN activity, especially in AGNs where the central region is hidden from direct view (Netzer 2013).

### 2.1.2 Classification

Next to the classical Hubble classification, AGN get classified in subgroups based on their spectral features, which are strongly dependent to their intrinsic structure. The key parameters for this classification are luminosity, emission-line profiles and radio properties. Based on those parameters AGN get grouped into Seyfert galaxies, quasars and radio galaxies. Seyfert galaxies are further subdivided based on the appearance of broad and narrow emission lines. Seyfert I galaxy spectra show both broad and narrow emission lines, while Seyfert II galaxy spectra show only narrow emission lines. Besides those main classes there are additional sub-classes including narrow-line Seyfert I galaxies (NLS1s), low-ionization nuclear emission-line regions (LINERs), and jet-dominated sources such as BL Lac objects or blazars (Antonucci 1993; C. Megan Urry and Padovani 1995).

#### Seyfert Galaxies

Seyfert galaxies are named after Carl K. Seyfert, who in 1943 observed spiral galaxies characterized by exceptionally bright nuclei and strong emission lines in their optical spectra (Seyfert 1943). They classified mainly the sub-classes Seyfert I and Seyfert II based on the presence of broad emission lines. Figure 2.2 highlights the differences of the spectra of Type I and Type II Seyfert galaxies.

Seyfert I galaxies, like NGC 4593, show both broad and narrow emission lines in their optical spectra. The broad lines, such as  $H_\alpha$  and  $H_\beta$ , have a full width at half maximum (FWHM) of typically several thousand kilometers per second and arise from the high-velocity BLR. In contrast, narrow lines, including prominent forbidden transitions like [O III]  $\lambda 5007$  or [N II]  $\lambda 6584$ , originate from the lower-velocity NLR (Osterbrock 1989; Bradley M. Peterson 1997). The presence of both components in the spectrum allows for a clear classification as a Seyfert 1 galaxy, which is the case for NGC4593. More to NGC4593 in section 3.1.

In comparison, Seyfert II galaxies lack these broad components in their optical spectra, likely due to orientation-dependent obscuration by the dusty torus. So



Figure 2.2: An example of Seyfert I and Seyfert II spectra illustrating their differences. Broad lines, such as the highlighted  $H\alpha$  and  $H\beta$ , are only present in the Seyfert I spectrum, whereas forbidden [O III] lines are visible in both cases. Adopted from (Runco 2015).

the classification of a Seyfert galaxies strongly depends on the viewing angle of the observer, which is the key point for the Unified Model of AGN, which will be discussed in section 2.1.3.

Another notable subclass are the so-called narrow-line Seyfert 1 galaxies (NLS1s). Despite their classification as Seyfert 1, the broad permitted lines in their spectra exhibit unusually small widths, with  $\text{FWHM} < 2000 \text{ km s}^{-1}$ . They often show strong Fe II emission complexes and steep soft X-ray spectra. NLS1s are thought to have low-mass black holes accreting at high Eddington rates, suggesting they may represent a young evolutionary phase of AGN activity (Osterbrock and Pogge 1985; Netzer 2013).

## Others

Next to Seyfert galaxies, there are several other classes of AGN. Quasars, which stands for quasi-stellar radio sources, are even more luminous than Seyfert galaxies and are typically found at higher redshifts. While the host galaxies of Seyfert galaxies are still observable, quasars completely outshine their host galaxies. Since quasars show similar emission characteristics to Seyfert galaxies, the modern distinc-

tion is based mainly on luminosity: quasars are classified as high-luminosity AGNs, while Seyfert galaxies represent the lower-luminosity end (Netzer 2013).

Radio galaxies are defining another AGN class. They are characterized by their strong radio emission and prominent jets, often associated with elliptical host galaxies. When their jets are aligned close to our line of sight, they are observed as blazars or BL Lac objects, which exhibit rapid variability and featureless optical spectra due to relativistic beaming (Netzer 2013).

Finally, LINERs are low-luminosity AGNs with spectra dominated by low-ionization emission lines. The physical origin of their ionization mechanism is still debated, and in some cases, they may not be powered by accretion at all (Netzer 2013).

While these classifications are based primarily on spectral characteristics, many of the observed differences between AGN types can be attributed to orientation effects. The Unified Model of AGN provides a framework that explains this apparent diversity through a common internal structure, viewed from different angles.

### 2.1.3 Unification Model

Figure 2.3 shows an illustration of the Unification Model, which was postulated by Robert Antonucci in 1993. He proposed that the visible differences in AGN spectra are not due to fundamentally different structures. Instead, they arise mainly from the viewing angle toward the AGN center and from obscuration by the dusty torus (Antonucci 1993).

The figure shows with what type the same AGN would get classified depending on the observer's viewing angle. Like mentioned before, the dusty torus plays a key role here, as it surrounds the central region of the AGN, the accretion disk and the fast-moving BLR. If the observer's line of sight is blocked by the torus, only radio emission and narrow-line emission from the NLR outside the torus can be detected. In this case, the AGN appears as a Seyfert 2 galaxy, since the broad emission lines from the BLR and the optical/UV radiation from the accretion disk are obscured. The observer essentially views the AGN from a flat angle, looking directly at the torus.

If, on the other hand, the observer has a direct view into the central region of the AGN, not obscured by the torus, the fast moving gas clouds of the BLR as well as the optical/UV emission continuum from the accretion disk become visible. So both, broad and narrow emission lines, can be observed, which classifies it as a Seyfert 1 Galaxy (Antonucci 1993).

The same principle applies to other AGN classes. Quasars can be considered the

high-luminosity counterparts of Seyfert galaxies, where orientation and torus obscuration likewise affect their observed properties. Blazars, on the other hand, are seen when the relativistic jet is aligned closely with the observer's line of sight, leading to strong Doppler boosting, which makes the radiation appear significantly brighter and shifted to higher frequencies than it intrinsically is (C. Megan Urry and Padovani 1995).

Although the classical Unification Model treats AGN classification as fixed and purely geometry-driven, some AGNs have been observed to change their spectral type over time. These so-called "changing-look AGNs" demonstrate that a purely orientation-based interpretation, such as the Unification Model, cannot explain all observed phenomena. They suggest that intrinsic changes, such as variations in accretion rate or obscuring material, can also affect the classification (Ricci and Trakhtenbrot 2023).

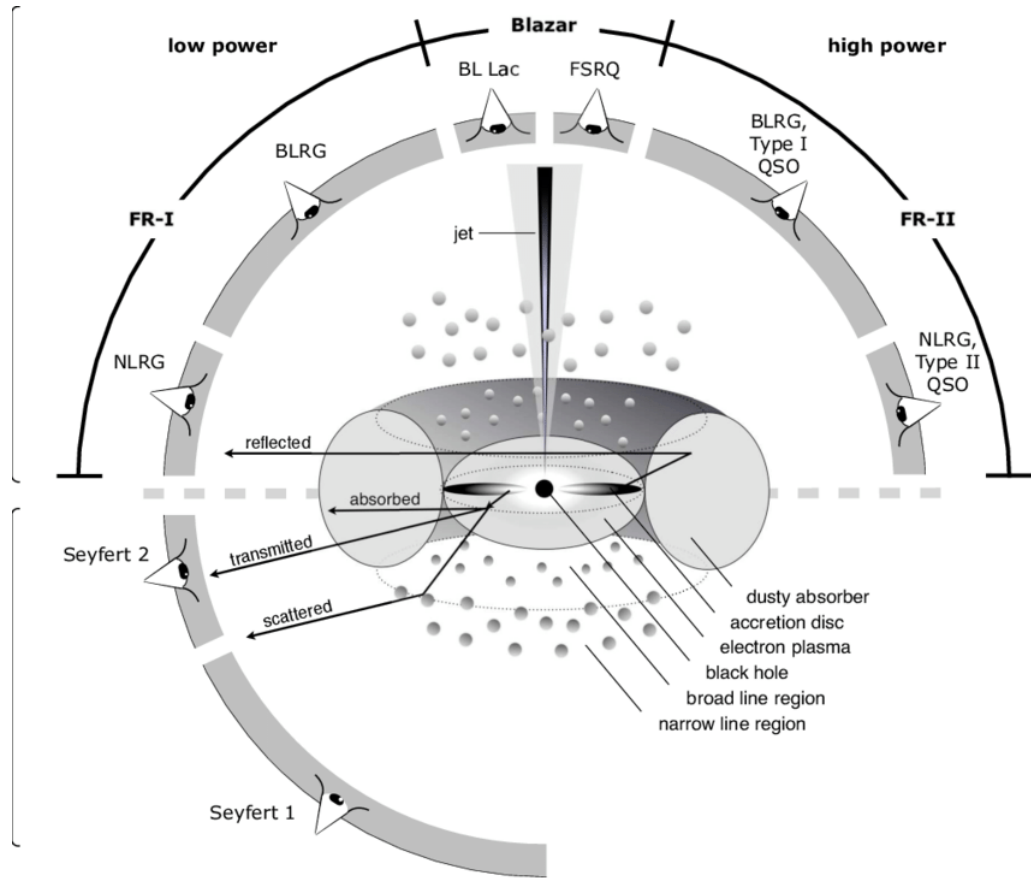


Figure 2.3: This graphic shows a schematic of the unification model of an AGN. The figure was adopted from (Beckmann and Shrader 2013).

### 2.1.4 Variability

Apart from changing-look AGNs that change their classification, many AGNs show significant and continuous variation in their emitted spectra. Unlike the much longer time period of changing-look AGNs, this variability can be observed over timescales of hours, days up to years across all the electromagnetic spectrum, with different fluctuation velocities. Averagely Higher-energy emission, like X-rays, shows faster and stronger variations than optical or infrared emission, which makes them energy-dependent. These timescales range from hours, to days and to years, showing generally a stochastic nature (Ulrich, Maraschi, and C Megan Urry 1997).

A way to explain the variability of an AGN are instabilities in the spiraling accretion flow onto the SMBH. Processes like magnetic turbulence in the corona, local fluctuations in the accretion rate or thermal inhomogenities within the disk could influence the continues accretion flow, creating fluctuation within the emitting regions. The energy-dependence can be understood considering the regions where the radiation originates from. High-energy emission arises from the innermost part of the accretion flow, mainly from the corona of the SMBH. It is a very compact region and the emitting volume is much smaller compared to the regions responsible for lower-energy emission, which are located at much larger radii. Following that, the light-crossing timescale  $t_l c = R/c$ , which defines how long light takes to pass the region, is much shorter for the compact high energy volume. In contrast to that, regions with larger radii, like the optical or infrared emitting regions, have much longer light-crossing timescale , resulting in correspondingly slower variability (Ulrich, Maraschi, and C Megan Urry 1997; I. M. McHardy et al. 2006).

Because of the variations being noticeable in small timescales, like hours ore days, it can be utilized to get more information about the size and the structure of emitting regions with an reverberation mapping analysis, which will be discussed in the next section.

## 2.2 Reverberation Mapping

The main focus of this work is a classic reverberation mapping analysis of the Broad Lines of NGC 4593. This observational technique allows to probe the structure of the BLR around the SMBH inside the AGN. This technique bases on the time delay or time lag between the continuum's variation and the correlated response of the broad lines. With this calculable time lag it is possible to assume the geometry of the BLR and calculating the mass of the SMBH.

### 2.2.1 Principle

The fundamental assumption in reverberation mapping is that fluctuations in the observed continuum luminosity drive corresponds to the fluctuations in the emission-line flux, with a measurable time delay. Like mentioned earlier, continuum fluctuations from the accretion disk serve as the ionizing source, illuminating the surrounding BLR. With variation in the continuum luminosity, the emission-line response follows these continuum variations with a measurable time lag (E. M. Cackett, M. C. Bentz, and Kara 2021). This time lag  $\tau$  is corresponding to the average light-travel distance from the photoionization continuum to the line emitting regions. Furthermore it is possible to approximate the characteristic radius of the BLR depending on  $\tau$  following this approximation:  $R_{\text{BLR}} \approx c \cdot \tau$ . With different time lags from emission lines origination from different regions it is possible to infer the geometry of the BLR. A BLR with a thin shell of clouds would produce a more uniform lag, whereas a broad distribution of clouds produces a range of lags. In principle, reverberation mapping can be used to 'map' the BLR's structure by inverting the delays (Bradley M. Peterson 1997). The response of the BLR's lines is typically assumed as linearly related to the photo-ionization continuum, leading to the convolution expression:

$$L(t) = \int \Psi(\tau) C(t - \tau) d\tau \quad (2.1)$$

where  $\Psi(\tau)$  is the transfer function, delivering the BLR's geometric and kinematic information (Keith Horne et al. 2004). While in theory the response of the BLR can be fully described by the transfer function  $\Psi(\tau)$ , this thesis focuses on measuring the time lag between continuum and line variations. This lag can be estimated using cross-correlation techniques, which are discussed in the following section.

### 2.2.2 Cross-Correlation Function and Lag Measurement

In practice, recovering the full transfer function  $\Psi(\tau)$  would require very well-sampled and high signal-to-noise light curves over a duration much longer than the expected lag. Since real monitoring campaigns are often affected by observational gaps and noise, such reconstructions are rarely possible (Keith Horne et al. 2004; B. M. Peterson 1993). For this reason, this thesis concentrates on measuring the mean time lag between continuum and emission-line variations using the Interpolated Cross-Correlation Function (ICCF) method.

Measuring the same objects over a span of time, it is possible to determine the cor-

relation coefficient (CCF) as a function of the time shift  $\tau$  between two light curves, e.g. the variable light curve of the ionizing continuum and the light curve of a broad emission line. By sliding one curve relative to the other, the ICCF quantifies how well the variations match for each lag. In this context, two types of lags are defined: the lag corresponding to the maximum correlation  $\tau_{\text{peak}}$  and the centroid lag  $\tau_{\text{centroid}}$ .  $\tau_{\text{centroid}}$  gets calculated over all points of the CCF, that are above a selected threshold which is typically 80% of the CCF. Since the centroid lag is generally considered a more robust representation of the mean light-travel time of the BLR (B. M. Peterson, Ferrarese, et al. 2004), it is used in this thesis.

The uncertainty of the measured lag is estimated using a Monte Carlo approach combining Flux Randomization (FR) and Random Subset Selection (RSS) (B. M. Peterson, Wanders, et al. 1998; B. M. Peterson, Ferrarese, et al. 2004). In the FR step, each flux value is randomly perturbed according to its measurement uncertainty. In the RSS step, a subset of the data points is drawn at random with replacement, preserving the original sample size. For each realization, the ICCF analysis is repeated, resulting in a distribution of centroid lags. The median of this distribution is adopted as the final lag measurement, while the 16th and 84th percentiles are taken as the  $1\sigma$  confidence interval, accounting for both measurement noise and the effects of uneven temporal sampling.

### 2.2.3 Black-Hole Mass

With the measured rest-frame centroid lag  $\tau_{\text{centroid}}$  from the ICCF analysis and the velocity width of the broad emission line, the mass of the central supermassive black hole (SMBH) can be estimated under the assumption that the BLR gas is gravitationally bound and its motions are dominated by the SMBH potential (B. M. Peterson, Ferrarese, et al. 2004). The distance to the BLR is given by

$$R_{\text{BLR}} = c \cdot \tau_{\text{centroid}} \quad (2.2)$$

and, combined with the line-of-sight velocity dispersion  $\Delta V$  of the BLR gas, the virial product is defined as:

$$M_{\text{vir}} = \frac{R_{\text{BLR}} \Delta V^2}{G}. \quad (2.3)$$

The physical black hole mass is then obtained by applying a scale factor  $f$ , which accounts for the unknown geometry, kinematics, and inclination of the BLR:

$$M_{\text{BH}} = f \cdot M_{\text{vir}}. \quad (2.4)$$

Following Onken et al. (2004), a mean value of  $f$  is adopted, calibrated by aligning reverberation-based masses with the  $M_{\text{BH}} - \sigma_*$  relation observed in not-active galaxies. Here,  $\sigma_*$  describes the stellar velocity dispersion of the galactic bulge. The actual scale factor can still vary between individual AGN because of differences in their geometry and orientation, which results in systematic uncertainties in the SMBH mass estimation. Still, the calibration of  $f$  against  $M_{\text{BH}} - \sigma_*$  delivers a well-established method for estimating the SMBH mass and will be used in this thesis.

## 2.3 Bowen Fluorescence

The mechanism known as Bowen Fluorescence was first described by I.S. Bowen in 1934 to explain unexpected emission lines in nebular spectra (Bowen 1934). It is a multi-stage process called resonant line pumping. In this process Photons, emitted by an ion, hits randomly another ion of a different species with a matching permitted transition, and excites it via absorption due to a near-wavelength coincidence. The resulting de-excitation leads to enhanced emission lines that would otherwise be too weak to detect through normal recombination or collisional excitation. In AGN, Bowen Fluorescence typically involves HeII Lyman- $\alpha$  photons at 303.78Å, which excite OIII ions and, in a secondary step, NIII ions. The result is the emission of characteristic ultraviolet and optical lines with similar correlation (Selvelli, Danziger, and Bonifacio 2007).

Similar fluorescence processes are also known for other ions. In this thesis, particular focus is placed on the OI $\lambda$ 8446 emission line. Its strength cannot be explained by recombination processes alone and is commonly attributed to Ly $\beta$  fluorescence. In this process, hydrogen Ly $\beta$  photons at 1025.72Å are absorbed by neutral oxygen due to a near-resonant transition. This enhances the OI emission through a separate, but related, fluorescence mechanism (Grandi 1980).

Although Ly $\beta$ -pumped OI $\lambda$ 8446 emission is independent of the classical Bowen mechanism, both processes share the fundamental principle of resonant line pumping, where photons from one species excite another species. As a result, both mechanisms provide valuable diagnostic information about the physical conditions and radiation field in AGN broad-line regions (Grandi 1980; Selvelli, Danziger, and Bonifacio 2007). In this work, the OI $\lambda$ 8446 emission line is investigated in the context of possible fluorescence excitation in NGC 4593.

## 3. Campaign and Analysis

The analysis of this campaign is based on the observation campaign of NGC4593 in 2016 by Edward M. Cackett (Edward M Cackett et al. 2018). This campaign took place between the 12th of July and the 6th of August with daily observations, which resulted in 26 successful out of 27 observations. It was performed with the Hubble Space Telescope (HST) using the Space Telescope Imaging Spectrograph (STIS) with the three different Gratings. The following section will cover an overview of the properties and specifications of NGC4593 and the campaign in 2016.

### 3.1 NGC4593

NGC 4593 is an active galactic nucleus (AGN), classified as a Seyfert 1 galaxy with a (R)SB(rs)b barred spiral morphology. It is located in the southern sky at RA = 12:39:39.44, DEC =  $-05^{\circ}20'39.03''$  (J2000) and has a redshift of  $z = 0.0083 \pm 0.0005$ , corresponding to a distance of about 35.6 Mpc (SIMBAD 2025) based on the  $\Lambda$ CDM model. The galaxy exhibits a prominent large-scale bar and nuclear dust ring connected to dust lanes along the bar, which likely channel gas toward the central region (Mulchaey and Regan 1997), as seen in figure 3.1. ALMA observations, conducted by (Garcia-Burillo et al. 2019), reveal a central molecular gas reservoir of  $\sim 10^8 M_{\odot}$  arranged in a one armed spiral and a circumnuclear ring, as well as evidence for a mild molecular outflow on scales of a few hundred parsecs, highlighting the interplay between a bar driven inflow and an AGN feedback in this galaxy.

The AGN of NGC4593 shows strong broad emission lines in H $\alpha$ , H $\beta$ , H $\gamma$ , Ly $\alpha$ , He I, and He II (Misty C Bentz and Katz 2015), indicating a well-developed broad-line region. It has a apparent magnitude of  $B = 13.95$  mag and  $V = 13.15$  mag (Véron-Cetty and Véron 2010) which gives a color index of  $(B - V) = 0.80$  mag. Near-infrared photometry shows emission as well in the  $J$ ,  $H$ , and  $K$  bands with  $J = 8.96 \pm 0.02$  mag,  $H = 8.29 \pm 0.02$  mag, and  $K = 7.98 \pm 0.03$  mag (Skrutskie and al. 2006), illustrating the broad spectral energy distribution emitted by the AGN.

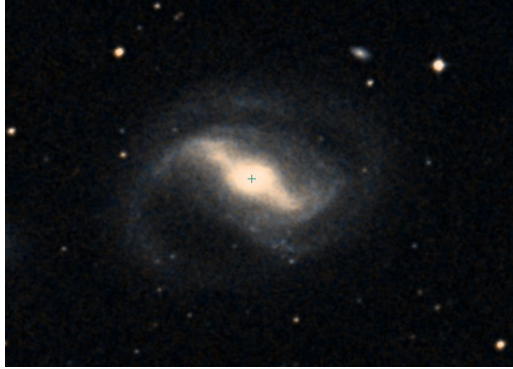


Figure 3.1: A DSS image of NGC4593.

Earlier reverberation mapping campaign based these broad lines showed a supermassive black hole mass of about  $M = (7.63 \pm 1.62) \times 10^6 M_{\odot}$  (Misty C Bentz and Katz 2015), which corresponds to a broad-line region radius of only a few light-days (Denney et al. 2006). Furthermore NGC4593 shows strong variability from X-ray to optical bands, with time delays that indicate a UV/optical-emitting accretion disk about three times larger than predicted by standard thin-disk theory and signatures of diffuse continuum emission from the BLR (Edward M Cackett et al. 2018).

## 3.2 2016 Campaign by E. M. Cackett

E. M. Cackett's campaign was designed to study wavelength dependent continuum lags. Therefore, the STIS instrument on the Hubble Space Telescope was used with low-resolution gratings to measure a broad range of wavelengths. In each observation, spectra were taken using three different gratings: G140L, G430L, and G750L. These were used together with the  $52'' \times 0.2''$  slit.

The characteristics of the STIS gratings used in this analysis are summarized in Table 3.1. After a standard pipeline-processing, a package was used to do a Charge Transfer Inefficiency correction with an algorithm based on (Anderson and Bedin 2010). The few left rest of hot pixels got manually removed by interpolating the flux of neighbor pixels.

Table 3.1: Overview of STIS Grating Characteristics (Space Telescope Science Institute 2025)

<b>Grating</b>	<b>Range [Å]</b>	<b>Exp. Time [s]</b>	<b>Res. Power</b>	<b>Dispersion [Å/pixel]</b>
G140L	1119–1715	1234	~ 1000	0.6
G430L	2888–5697	298	~ 500 – 1000	2.73
G750L	5245–10233	288	~ 500 – 1000	4.92

### 3.3 Intercalibration and Determination of AVG and RMS Spectra

Reverberation mapping requires multiple epochs to capture variability. For the 2016 campaign of NGC 4593, we retrieved 27 spectra from the ... archive of which 26 are usable for further analysis. The top panel of Figure 3.2 shows a section between about 4000 Å and 9000 Å of the optical spectral range from these epochs.

For the subsequent analysis, the average spectrum (AVG) is obtained by averaging over all epochs. Ideally, this improves the signal-to-noise ratio (S/N) sufficiently to identify spectral features in NGC 4593. Furthermore it is essential for the reverberation mapping analysis to identify variability between the epochs, which can be obtained with the root-mean-square (RMS) spectrum, defined as the standard deviation of the flux at each wavelength across epochs:

$$F_{\text{RMS}}(\lambda) = \sqrt{\frac{1}{N-1} \sum_{i=1}^N [F_i(\lambda) - \bar{F}(\lambda)]^2}, \quad (3.1)$$

with the mean spectrum at wavelength  $\lambda$  given by

$$\bar{F}(\lambda) = \frac{1}{N} \sum_{i=1}^N F_i(\lambda). \quad (3.2)$$

Constant features, like narrow emission lines, vanishes in the RMS spectrum, whereas variable components, like broad emission lines stands out. The top panel of Figure 3.2 shows the AVG and RMS spectra from the original retrieved data. It shows, that residual variability remains in nominally non-varying lines, especially in the forbidden features near 5000 Å. This indicates small wavelength misalignment between epochs. Therefore an intercalibration anchored to the narrow [O III]  $\lambda 5007$  line was performed, by correcting the wavelengths of the spectra by a maximum of 1 Å. The lower panels of Figures 3.2 present the intercalibrated epochs and the corresponding AVG and RMS spectra. The disappearance of narrow features in the calibrated RMS spectrum, especially the [O III]  $\lambda 5007$  line, confirms that the apparent variability in the uncalibrated RMS was induced by the wavelength shifts between the epochs rather than intrinsic line variability. However the intercalibration was only applied to the optical part of the spectra due to its limited reliability. Following that the intercalibrated AVG and RMS spectra will be used for optical part, taken by the G430L and G750L gratings used in the following analysis and the uncalibrated AVG and RMS spectra for the emission lines in the UV part of

spectrum and their analysis, as they were taken by the G140L gratings.

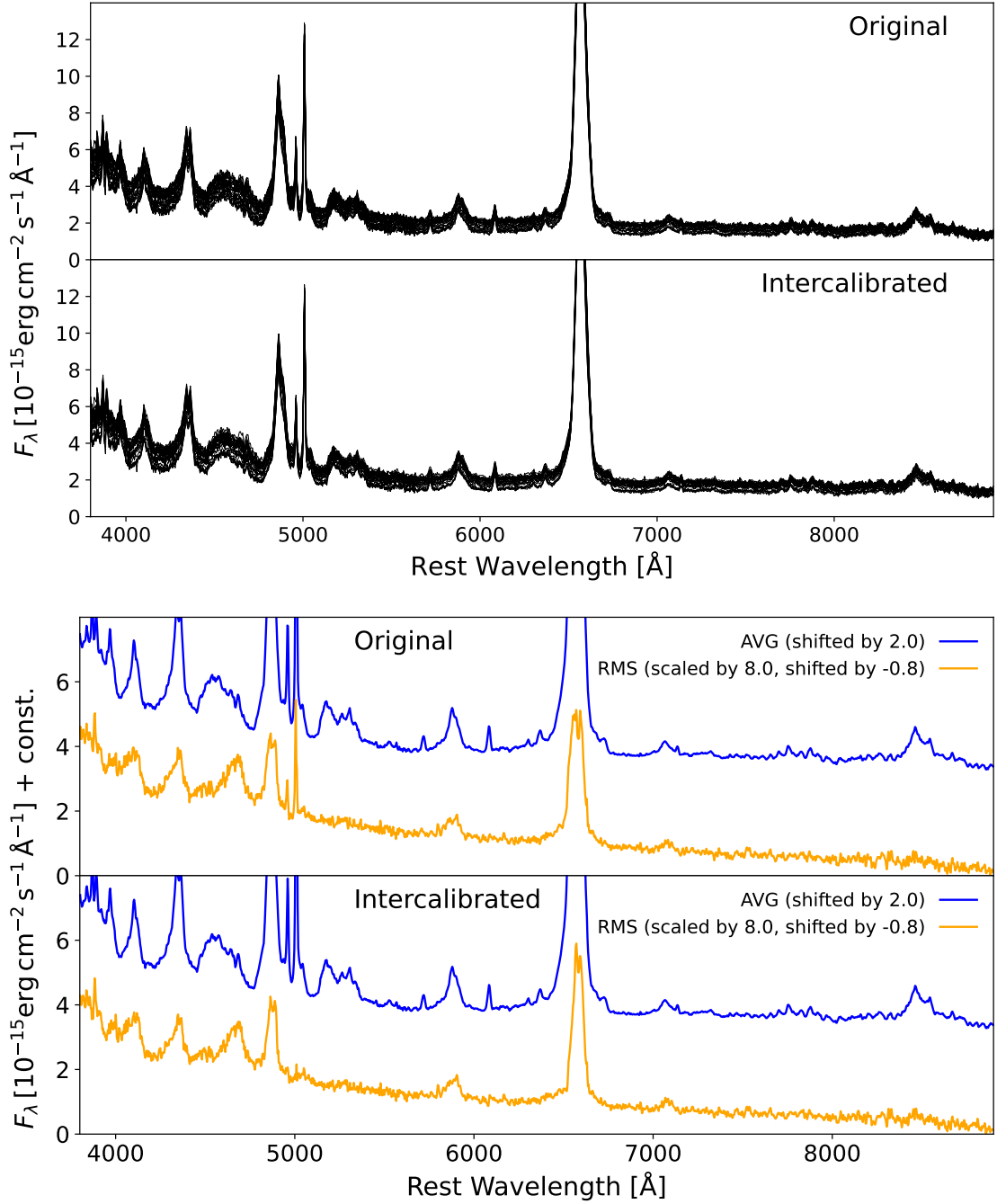


Figure 3.2: Comparison of the optical spectral range from the 2016 campaign of NGC 4593, showing the effects of [O III]  $\lambda 5007$  intercalibration on both the individual spectra (top) and the derived average and rms spectra (bottom).

## 4. Reverberation Mapping Analysis of NGC4593

### 4.1 Line Determination

Having obtained the AVG- and RMS spectrum of NGC4593, the next step is the identification of the emission lines. Figure 4.1 and 4.2 show the optical to near-infrared range between 3900Å and 9000Å and the UV range between 1100Å and 1700Å, respectively.

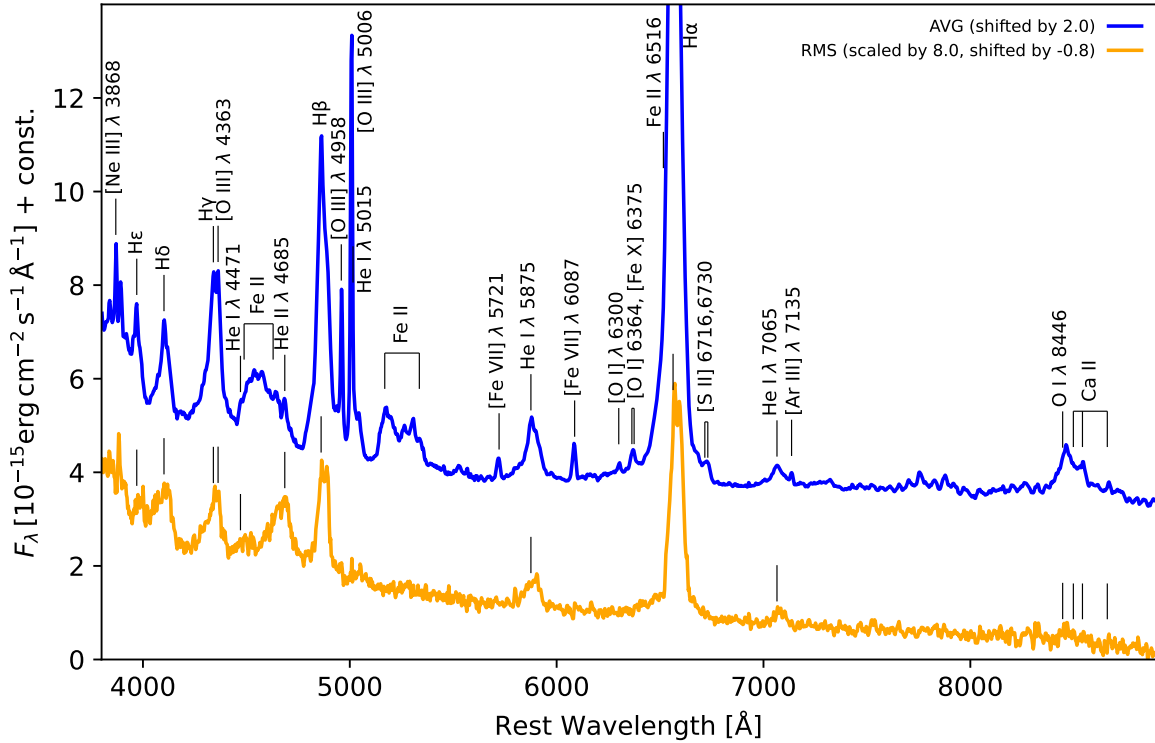


Figure 4.1: Optical AVG and RMS spectrum with determined emission lines.

Looking at Figure 4.1, the most prominent broad emission lines in the AVG spectrum are the Balmer-Lines, with  $\text{H}\alpha$  being the strongest followed by  $\text{H}\beta$  and  $\text{H}\gamma$ . Their variations are clearly visible in the RMS spectrum and the line profiles of  $\text{H}\alpha$  and  $\text{H}\beta$  in particular show strong similarities, which will be discussed in more detail later in this chapter. In addition to the Balmer emission lines there are several He-emission lines such as  $\text{He II } \lambda 4685$ ,  $\text{He I } \lambda 5875$  and  $\text{He I } \lambda 7065$  show measurable variability. Another significant broad emission line complex appears in the far-red part of the spectrum, including the  $\text{O I } \lambda 8446$  and  $\text{Ca II}$  lines. The  $\text{O I } \lambda 8446$  line is of particular interest in this thesis, as it shows variation which was never measured through a reverberation mapping analysis before.

Apart from the broad emission lines, the AVG spectrum also exhibits several strong forbidden emission lines with the  $[\text{O III}] \lambda 5007$  and the  $[\text{O III}] \lambda 4958$  as the most prominent ones. As mentioned in the previous chapter, the first one was used for the intercalibration of the spectra and, as expected, shows no variability in the RMS spectrum, similar to the other forbidden lines. Finally, the AVG spectrum shows additionally two Fe II emission line groups, that shows no variation in the RMS spectrum.

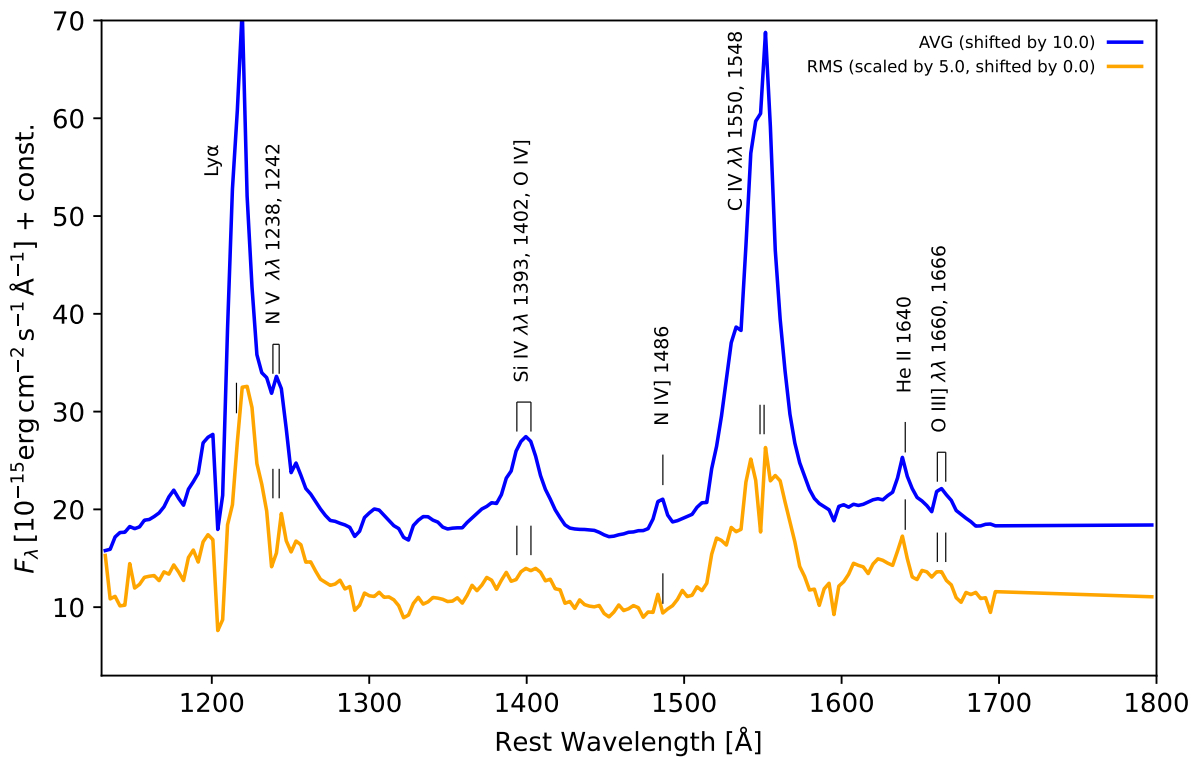


Figure 4.2: UV spectrum AVG and RMS spectrum with determined emission lines

The UV spectrum, shown in figure 4.2, contains only a few additional broad and semi-forbidden emission lines due to its limited coverage. In addition to the prominent Si and C broad emission lines, it shows strong and variable Ly $\alpha$  emission, which is of particular significance for this thesis.

The Bowen fluorescence of O I  $\lambda$ 8446, which is investigated in this analysis, is typical driven by the emission of the Ly $\beta$  line, which lies outside the spectral range of the HST Campaign. However, as can be seen in figure 4.2, Ly $\alpha$  still lies in the spectral range of the campaign, as the most blue broad line of the taken spectra. As Ly $\alpha$  and Ly $\beta$  are assumed to originate from the same physical region, Ly $\alpha$  can be used to examine the correlation of O I  $\lambda$ 8446 and Ly $\alpha$  for Bowen fluorescence.

## 4.2 Emission Line and Continua Measurement

After identifying the emission lines, the next step of the analysis is to calculate the fluxes of those lines. This is done with the help of a python-based tool called gecho, which uses methods for lag measurements and line-width measurements based on ... . With help of this tool the flux density gets integrated over the extent of each emission line for every observed spectrum of the campaign. Here it is important to define the integration limits so that only the variable component of the emission line is measured in this way To ensure this, a parallel view of the AVG- and RMS-spectrum was used to define those integration limits, by identifying the variable components of the line in the RMS-spectrum. Additionally, it must be ensured, that no component of any other line is contributing to the line flux of the measured line, which can lead to misleading conclusions. But before the line flux can be calculated, the surrounding continuum has to be subtracted, which can be done by interpolating a linear pseudo-continuum between sections on the blue and red side with no line contribution. The chosen integration limits and pseudo-continua can be found in Table 4.1. With the fluxes of each line now derived from all observed spectra, it is possible to extract the lightcurves of the measured emission line, which will be further covered in the next section.

Besides the emission line lightcurves, continua lightcurves from different wavelength ranges are needed for the further analysis. The extraction process is similar to the emission line lightcurves, except that they get calculated by the mean flux density of a sufficiently large region without line emission or absorption. Logically a pseudo-continua subtraction is not needed here. The chosen integration limits for the continua can be found in Table 4.2.

Table 4.1: Integration Limits and Pseudo-Continua of the measured emission lines

<b>Line</b>	<b>Integration Limits</b>	<b>Pseudo-Continua</b>
Ly $\alpha$	1207 – 1238	1151 – 1161, 1462 – 1468
H $\alpha$	6520 – 6634	6107 – 6129, 6861 – 6900
H $\beta$	4828 – 4924	4762 – 4774, 5085 – 5112
H $\gamma$	4317 – 4391	4197 – 4220, 4435 – 4450
HeI $\lambda$ 5875	5840 – 5941	5645 – 5653, 6044 – 6057
HeII $\lambda$ 4685	4610 – 4744	4435 – 4450, 4762 – 4774
OI $\lambda$ 8446	8380 – 8498	8005 – 8031, 8850 – 8955
OIII $\lambda$ 5007	4982 – 5033	4762 – 4774, 5085 – 5112

Table 4.2: Integration Limits of the measured continua

<b>Line</b>	<b>Integration Limits</b>
Cont. 1150	1151 – 1161
Cont. 4010	4026 – 4033
Cont. 4440	4435 – 4450
Cont. 5100	5085 – 5112
Cont. 6110	6107 – 6129
Cont. 6880	6861 – 6900
Cont. 8015	8005 – 8031
Cont. 8900	8864 – 8955

The variability of the emission lines and continua being the basis of a reverberation analysis, it is helpful to use variability statistics, as defined by Rodriguez-Pascual et al. 1997. Thus include the extrema of the flux densities of the emission lines as well as the extrema of the integrated fluxes of the continua  $F_{\min}$  and  $F_{\max}$ , the ratio of the maximum and minimum flux  $R_{\max}$ , the mean flux  $\langle F \rangle$ , the standard deviation  $\sigma_F$  and finally the fractional variation, which is defined as:

$$F_{\text{var}} = \frac{\sqrt{\sigma_F^2 - \Delta^2}}{\langle F \rangle} \quad (4.1)$$

Here  $\Delta^2$  is the mean square value of the uncertainties of the fluxes defined as:

$$\Delta^2 = \frac{1}{N} \sum_N^{i=1} \Delta_i^2 \quad (4.2)$$

The results of these parameters can be found in table 4.3.

Table 4.3: Variability statistics of the investigated continua and broad lines with minimum (2) and maximum flux density or integrated flux (3), peak-to-peak ratio (4), mean (5), standard deviation (6) and fractional variation (7).

Continuum/Line (1)	$F_{\min}$ (2)	$F_{\max}$ (3)	$R_{\max}$ (4)	$\langle F \rangle$ (5)	$\sigma_F$ (6)	$F_{\text{var}}$ (7)
Cont. 1150	0.52	1.35	2.58	0.86	0.25	0.28
Cont. 4010	2.68	4.21	1.57	3.49	0.47	0.14
Cont. 4440	2.42	3.73	1.54	3.14	0.39	0.12
Cont. 5600	1.36	2.15	1.59	1.82	0.25	0.14
Cont. 6110	1.49	2.27	1.53	1.9	0.23	0.12
Cont. 6880	1.33	2.01	1.5	1.72	0.2	0.11
Cont. 8015	1.18	1.69	1.43	1.48	0.15	0.1
Cont. 8900	1.14	1.52	1.33	1.38	0.11	0.08
Ly $\alpha$	66.87	94.88	1.42	82.21	8.03	0.1
H $\alpha$	112.34	129.72	1.15	122.03	4.36	0.04
H $\beta$	32.7	39.12	1.2	36.49	1.77	0.05
H $\gamma$	14.45	17.85	1.24	16.5	0.94	0.06
HeII $\lambda$ 4685	5.53	9.81	1.77	7.73	1.37	0.18
HeI $\lambda$ 5875	6.81	9.54	1.4	8.49	0.62	0.07
OI $\lambda$ 8446	7.47	9.13	1.22	8.32	0.37	0.04
OIII $\lambda$ 5007	12.97	13.65	1.05	13.39	0.18	0.01
UVW2	-	-	-	-	-	0.125

## 4.3 Lightcurves

This chapter will cover the plots and comparison of the extracted emission line and continua lightcurves. Additionally to the measured lightcurves, the UVW2 continuum lightcurve from the swift campaign taken by (I. McHardy et al. 2018) is included in the further analysis, as it was used by E. Cackett in his analysis too (Edward M Cackett et al. 2018).

### 4.3.1 Continua

First looking at the continua lightcurves in figure 4.3, it shows that they follow a similar overall shape. All lightcurves start with a pronounced maxima, which shows in most cases the highest flux level, with exception of the 1150 continuum. This is followed by a significant flux minimum where the flux decreases by about 25 – 46% relative to the total flux maximum of the curve. From there the curves rise again toward another local maximum that nearly reaches the initial peak. In most

cases, this second maximum is composed of a higher plateau, a smaller plateau, and an additional peak, before the lightcurves steadily decline toward their overall flux minimum.

**Describe the selection of the Cont. 1015 continuum and the UVW2 continuum**

#### 4.3.2 Emission Lines

Like mentioned earlier, the lightcurves of the emission-lines H $\alpha$ , H $\beta$ , H $\gamma$ , Ly $\alpha$ , HeI  $\lambda$ 5875, HeII  $\lambda$ 4685 and OI  $\lambda$ 8446 where selected for the further reverberation mapping analysis. Figure 4.4 and 4.5 show those lightcurves compared to the selected blue continuum Cont. 1150 and respectively compared to the external swift continuum UVW2. This comparison shows strong similarities between the continua and emission-line lightcurves, as most features of the 1150 and UVW2 continuum lightcurves can be found in the emission-line curves too, shifted within a few days.

**create comparison figures for this lightcurves**

### 4.4 Line Profiles

### 4.5 Time Lag and BH Masses

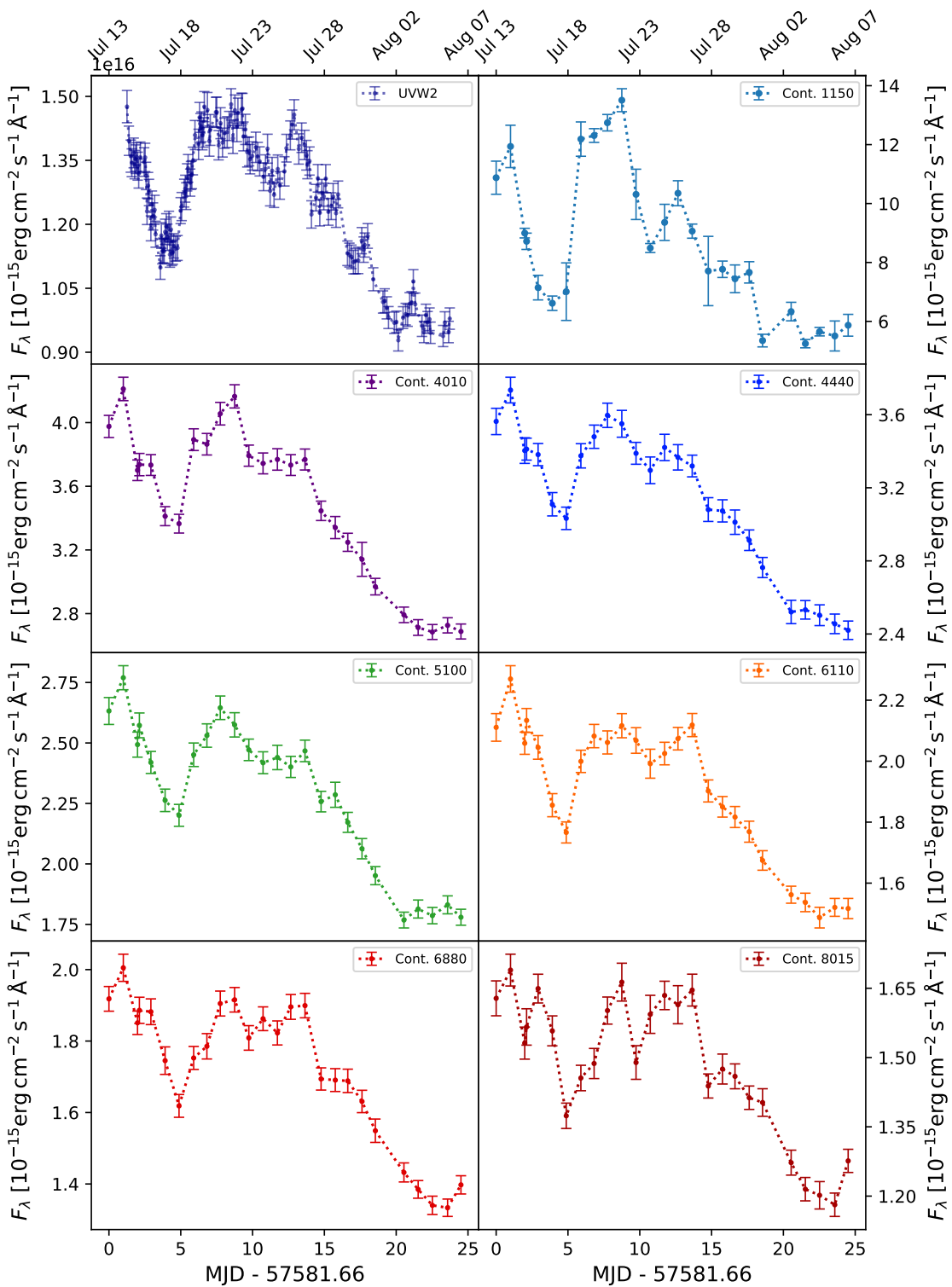


Figure 4.3: ...

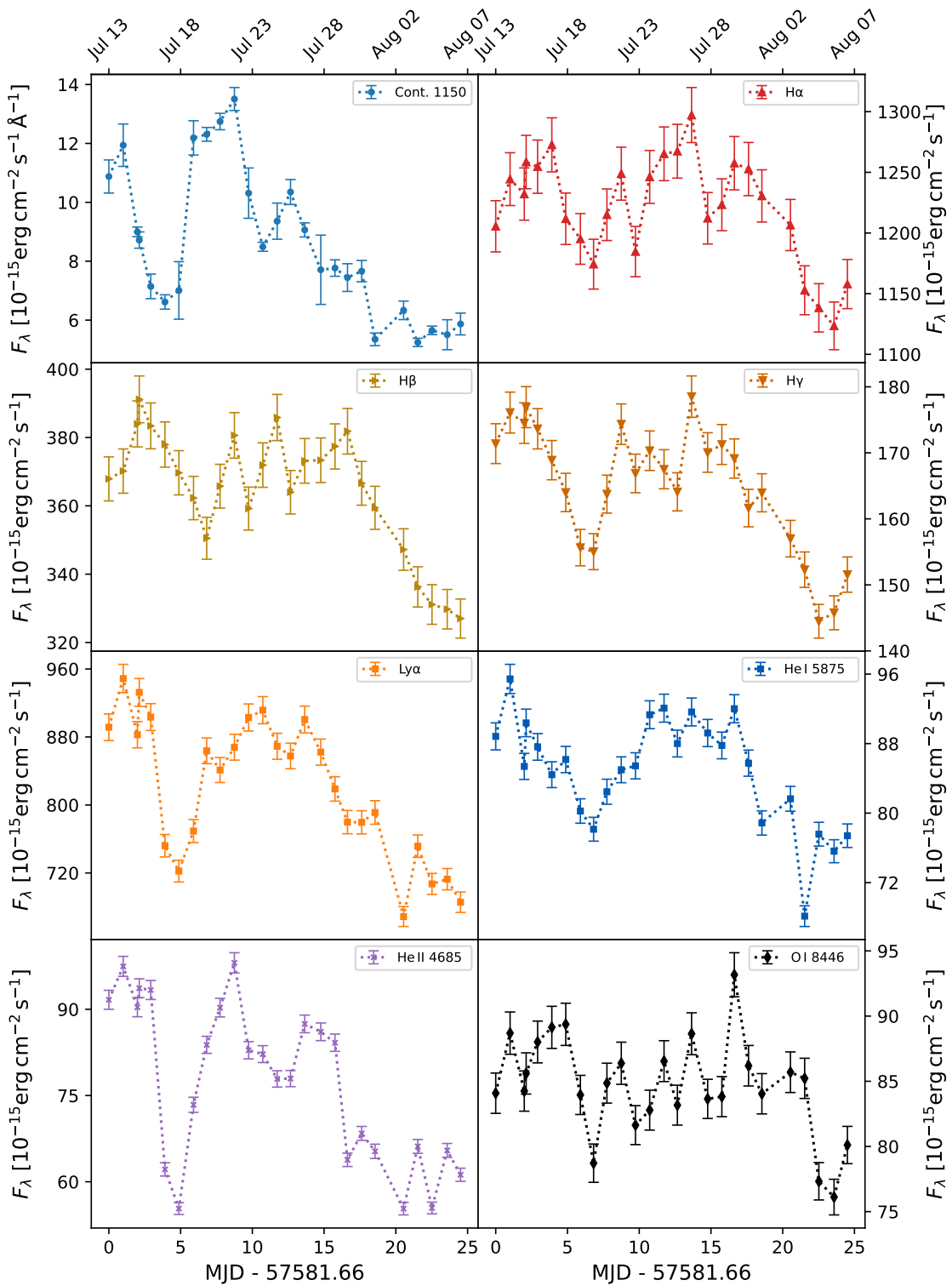


Figure 4.4: AVG RMS Spektrum

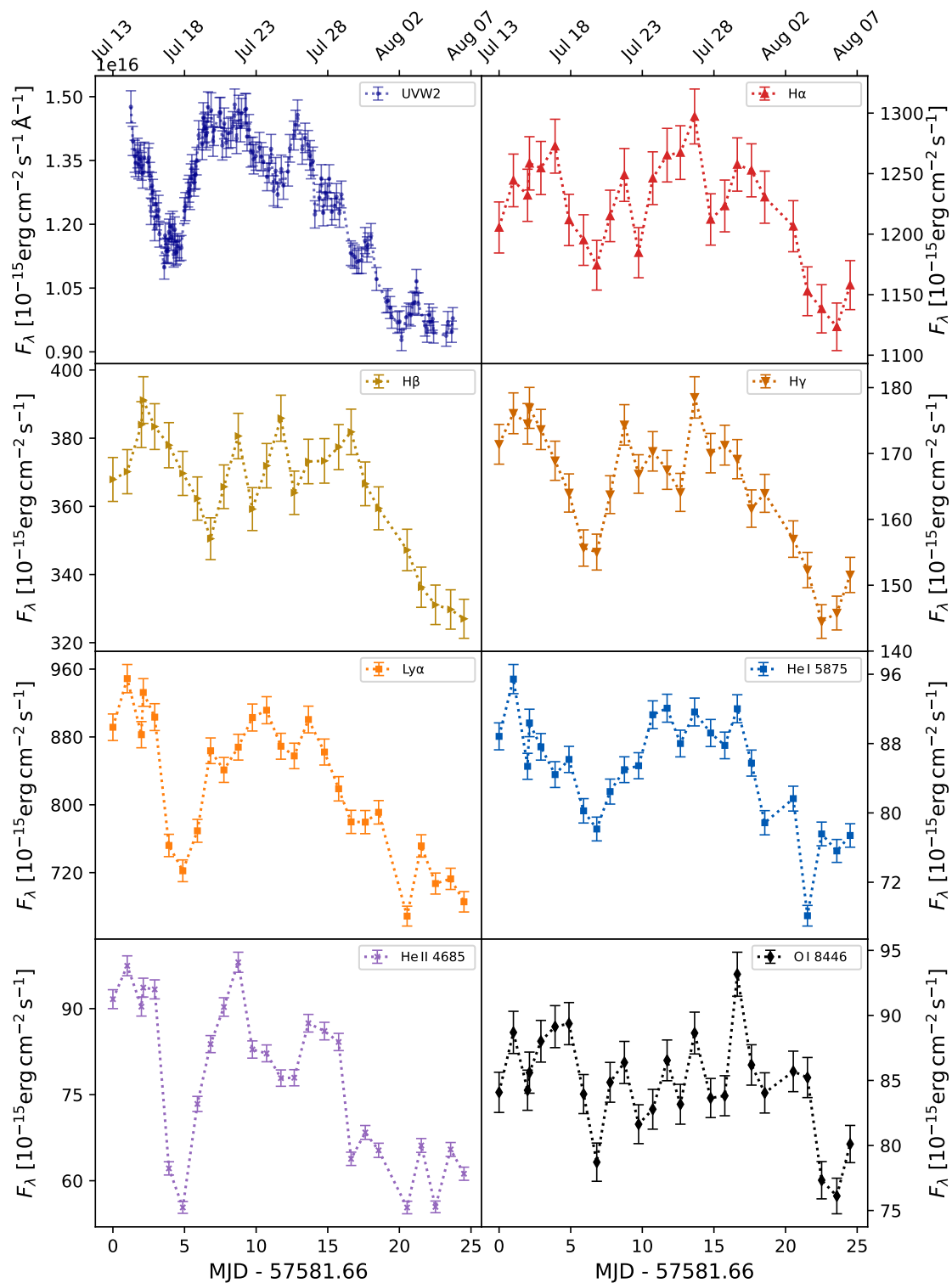


Figure 4.5: AVG RMS Spektrum

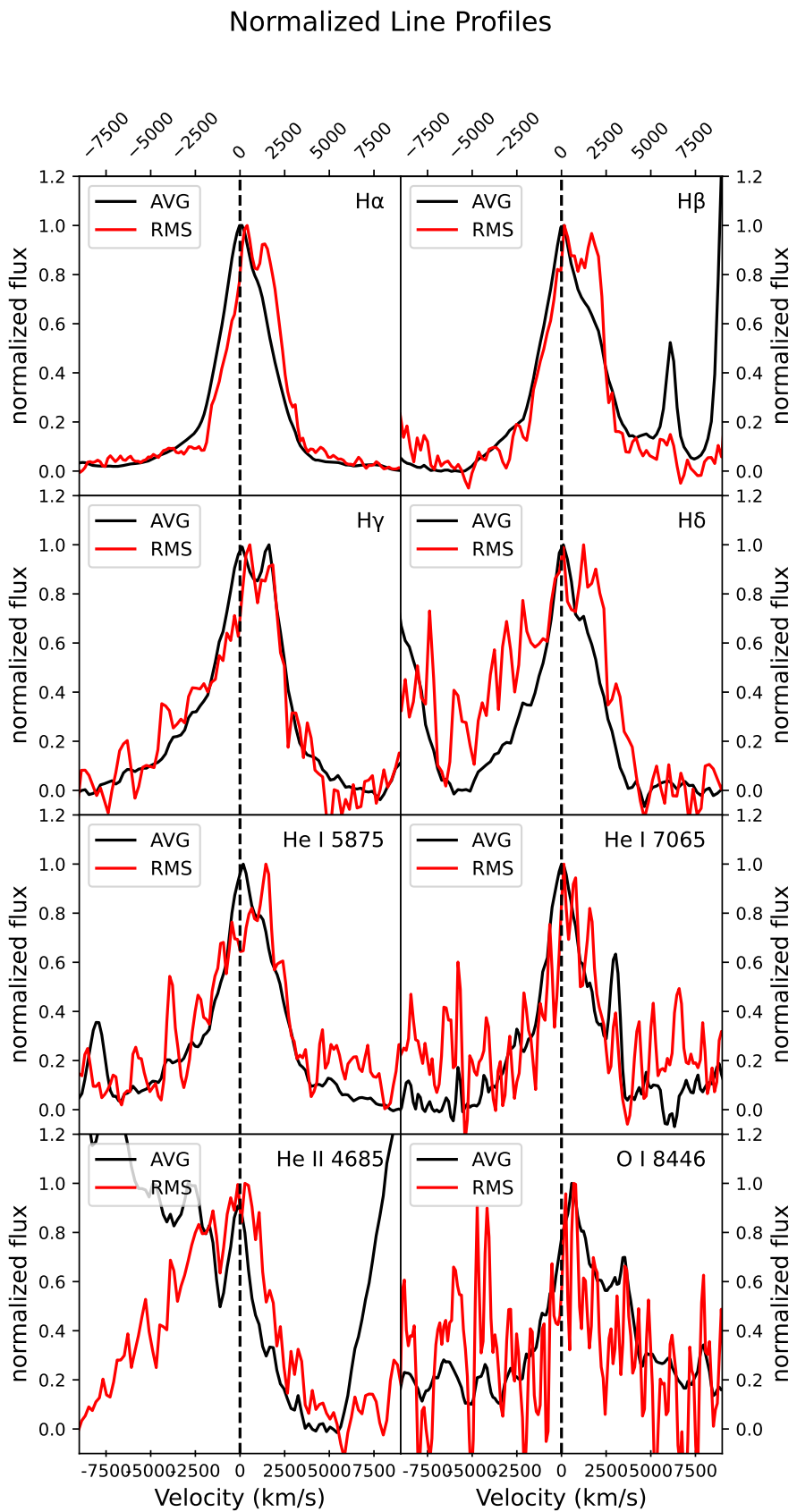


Figure 4.6: AVG RMS Spektrum

### CCFs between Emission Lines and UVW2 for NGC4593

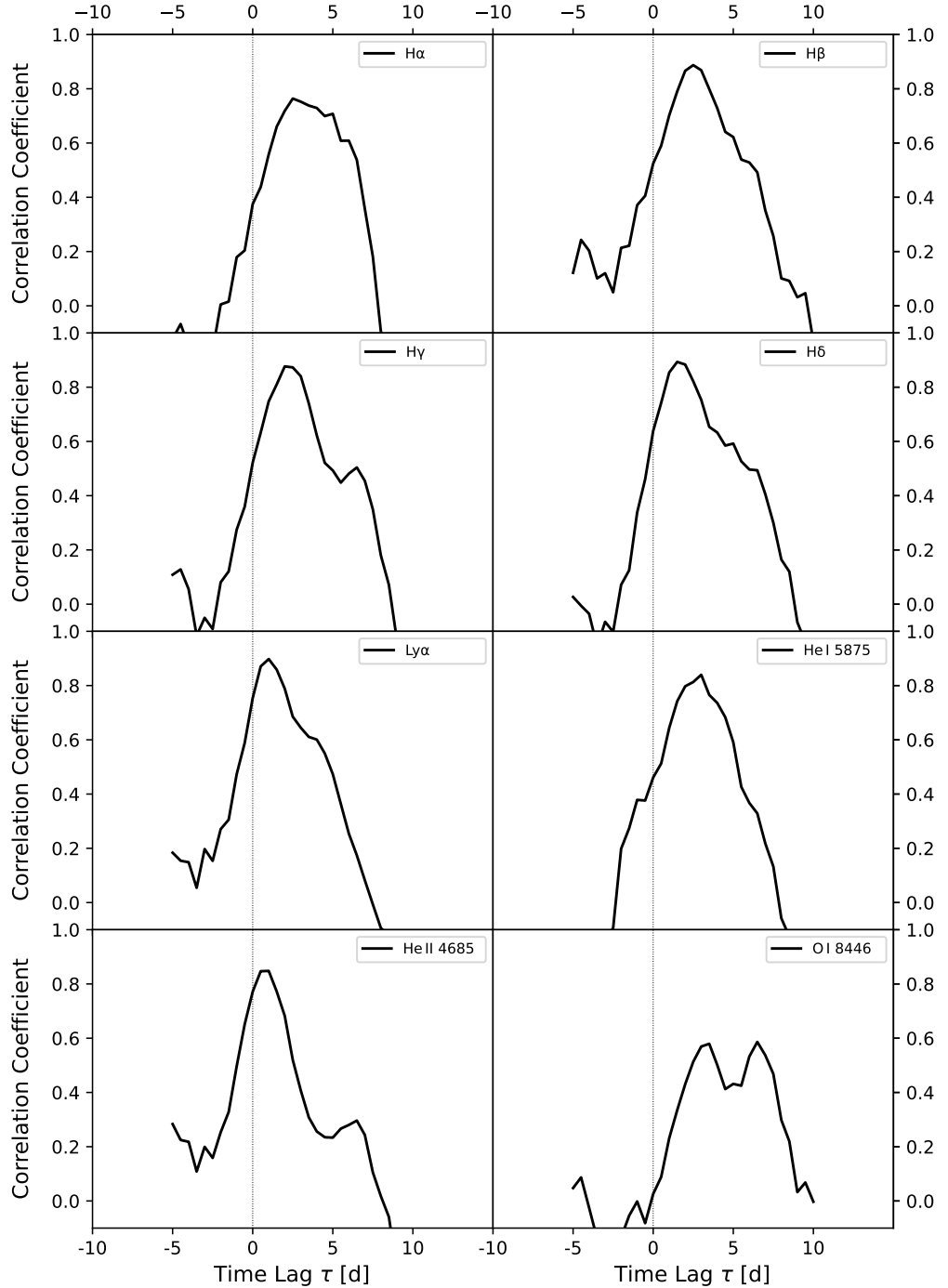


Figure 4.7: AVG RMS Spektrum

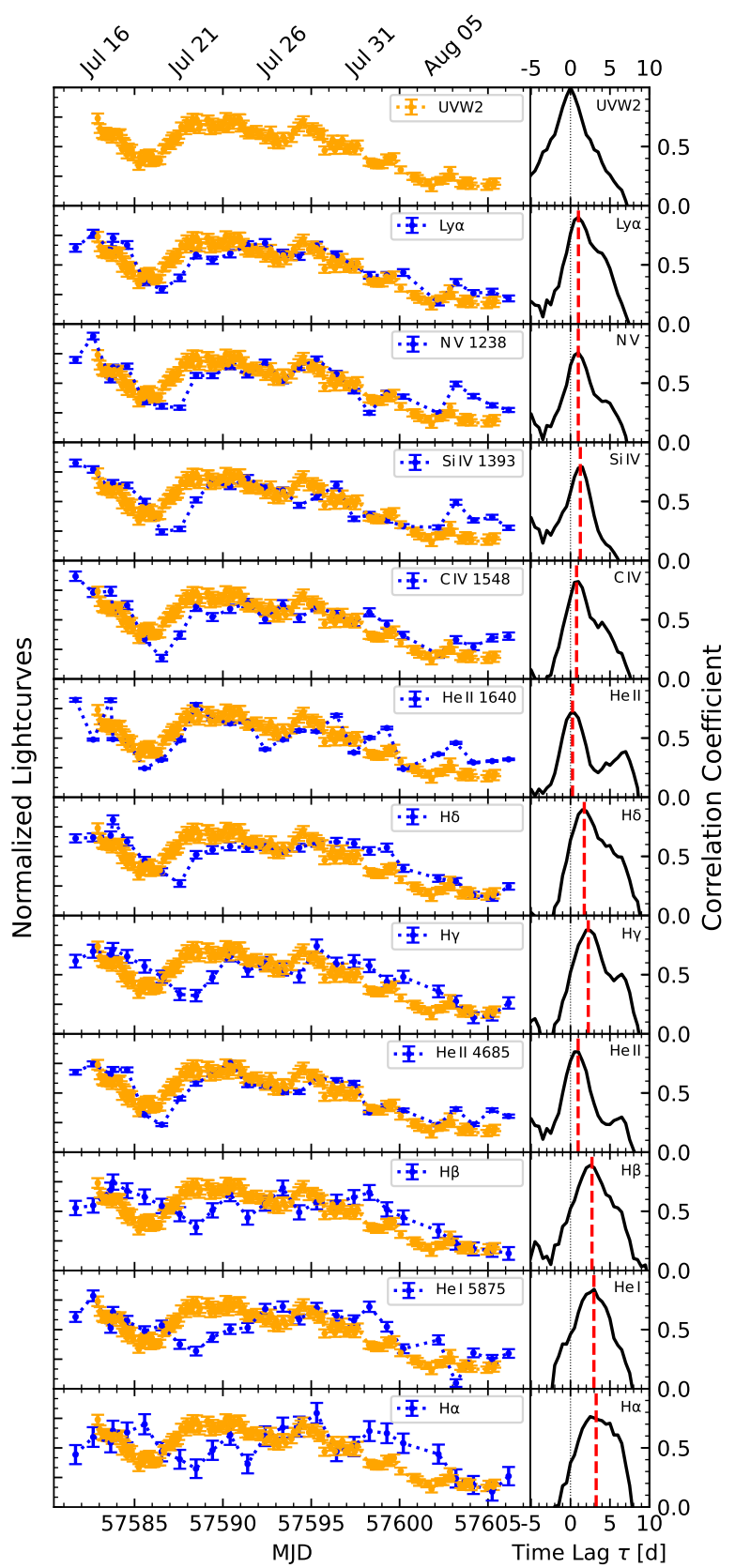


Figure 4.8: AVG RMS Spektrum

## 5. Discussion

# Bibliography

- Anderson, Jay and Luigi R Bedin (2010). “An empirical pixel-based correction for imperfect cte. i. hst’s advanced camera for surveys1”. In: *Publications of the Astronomical Society of the Pacific* 122.895, p. 1035.
- Antonucci, Robert (1993). “Unified models for active galactic nuclei and quasars”. In: *Annual Review of Astronomy and Astrophysics* 31, pp. 473–521. DOI: 10.1146/annurev.aa.31.090193.002353.
- Beckmann, Volker and Chris Shrader (Feb. 2013). “The AGN phenomenon: Open issues”. In: *Proceedings of Science*.
- Bentz, Misty C and Sarah Katz (2015). “The AGN black hole mass database”. In: *Publications of the Astronomical Society of the Pacific* 127.947, p. 67.
- Bowen, I. S. (1934). “The excitation of the permitted O III nebular lines”. In: *Publications of the Astronomical Society of the Pacific* 46.271, pp. 146–148.
- Cackett, E. M., M. C. Bentz, and E. Kara (2021). “Reverberation Mapping of Active Galactic Nuclei: From X-ray Corona to Dusty Torus”. In: *iScience* 24.12, p. 102557. DOI: 10.1016/j.isci.2021.102557.
- Cackett, Edward M et al. (2018). “Accretion disk reverberation with Hubble space telescope observations of NGC 4593: evidence for diffuse continuum lags”. In: *The Astrophysical Journal* 857.1, p. 53.
- Denney, Kelly D. et al. (Dec. 2006). “The mass of the black hole in the Seyfert 1 galaxy NGC 4593 from reverberation mapping”. In: *Astrophysical Journal Letters* 653, pp. 152–158. DOI: 10.1086/508533.
- Garcia-Burillo, S. et al. (2019). “ALMA images the many faces of the NGC1068 torus and its surroundings”. In: *Astronomy & Astrophysics* 632, A61. DOI: 10.1051/0004-6361/201936606.
- Grandi, S. A. (May 1980). “OI lambda 8446 emission in Seyfert 1 galaxies.” In: 238, p. 10. DOI: 10.1086/157952.
- Hickox, Ryan C. and David M. Alexander (2018). “Obscured Active Galactic Nuclei”. In: *Annual Review of Astronomy and Astrophysics* 56, pp. 625–671.

- Horne, Keith et al. (2004). “Observational Requirements for High-Fidelity Reverberation Mapping”. In: *Publications of the Astronomical Society of the Pacific* 116.819, p. 465.
- McHardy, I. M. et al. (2006). “Active galactic nuclei as scaled-up Galactic black holes”. In: *Nature* 444.7120, pp. 730–732. DOI: 10.1038/nature05389.
- McHardy, IM et al. (2018). “X-ray/UV/optical variability of NGC 4593 with Swift: reprocessing of X-rays by an extended reprocessor”. In: *Monthly Notices of the Royal Astronomical Society* 480.3, pp. 2881–2897.
- Mo, Houjun, Frank van den Bosch, and Simon White (2010). *Galaxy Formation and Evolution*. Cambridge University Press. ISBN: 9780521857932.
- Mulchaey, John S. and Michael W. Regan (June 1997). “The Fueling of Nuclear Activity: II. The Bar Properties of Seyfert and Normal Galaxies”. In: *The Astrophysical Journal Letters* 482.2, pp. L135–L138. DOI: 10.1086/310710.
- Netzer, Hagai (2013). *The Physics and Evolution of Active Galactic Nuclei*. Cambridge: Cambridge University Press.
- Onken, C. A. et al. (2004). “Supermassive Black Holes in Active Galactic Nuclei. II. Calibration of the Black Hole Mass-Velocity Dispersion Relationship for Active Galactic Nuclei”. In: *The Astrophysical Journal* 615, pp. 645–651. DOI: 10.1086/424655.
- Osterbrock, Donald E. (1989). *Astrophysics of Gaseous Nebulae and Active Galactic Nuclei*. Mill Valley, California: University Science Books. ISBN: 9780935702111.
- Osterbrock, Donald E. and Richard W. Pogge (1985). “The spectra of narrow-line Seyfert 1 galaxies”. In: *The Astrophysical Journal* 297, pp. 166–176. DOI: 10.1086/163513.
- Peterson, B. M. (1993). “Reverberation Mapping of Active Galactic Nuclei”. In: *Publications of the Astronomical Society of the Pacific* 105, pp. 247–268. DOI: 10.1086/133140.
- Peterson, B. M., L. Ferrarese, et al. (2004). “Central Masses and Broad-Line Region Sizes of Active Galactic Nuclei. II. A Homogeneous Analysis of a Large Reverberation-Mapping Database”. In: *The Astrophysical Journal* 613, pp. 682–699. DOI: 10.1086/423269.
- Peterson, B. M., I. Wanders, et al. (1998). “Optical Continuum and Emission-Line Variability of Seyfert 1 Galaxies”. In: *The Astrophysical Journal* 501, pp. 82–93. DOI: 10.1086/305813.
- Peterson, Bradley M. (1997). *An Introduction to Active Galactic Nuclei*. Cambridge University Press. ISBN: 9780521473484.

- Ricci, Claudio and Benny Trakhtenbrot (2023). “Changing-look active galactic nuclei”. In: *Nature Astronomy* 7.11, pp. 1282–1294.
- Rodriguez-Pascual, PM et al. (1997). “Steps toward determination of the size and structure of the broad-Line region in active galactic nuclei. IX. Ultraviolet observations of fairall 9”. In: *The Astrophysical Journal Supplement Series* 110.1, p. 9.
- Runco, Jordan (2015). “Frequency of Seyfert Type Transitions in a Sample of 102 Local Active Galactic Nuclei”. In.
- Selvelli, Pierluigi, John Danziger, and Piercarlo Bonifacio (2007). “The He Fowler lines and the O and N Bowen fluorescence lines in the symbiotic nova RR Telescopii”. In: *Astronomy & Astrophysics* 464.2, pp. 715–734.
- Seyfert, Carl K. (1943). “Nuclear Emission in Spiral Nebulae”. In: *The Astrophysical Journal* 97, pp. 28–40. DOI: 10.1086/144488.
- Shakura, N. I. and R. A. Sunyaev (1973). “Black holes in binary systems. Observational appearance”. In: *Astronomy and Astrophysics* 24, pp. 337–355.
- SIMBAD (2025). *NGC4593*. URL: <https://simbad.u-strasbg.fr/simbad/sim-id?Ident=NGC4593> (visited on 06/10/2025).
- Skrutskie, M. F. and et al. (2006). “The Two Micron All Sky Survey (2MASS)”. In: *The Astronomical Journal* 131, pp. 1163–1183. DOI: 10.1086/498708.
- Space Telescope Science Institute (2025). *STIS Instrument Handbook: Gratings*. URL: <https://hst-docs.stsci.edu/stisihb/chapter-13-spectroscopic-reference-material/13-3-gratings> (visited on 05/12/2025).
- Ulrich, Marie-Helene, Laura Maraschi, and C Megan Urry (1997). “Variability of active galactic nuclei”. In: *Annual Review of Astronomy and Astrophysics* 35.1, pp. 445–502.
- Urry, C. Megan and Paolo Padovani (1995). “Unified Schemes for Radio-Loud Active Galactic Nuclei”. In: *Publications of the Astronomical Society of the Pacific* 107.715, pp. 803–845. DOI: 10.1086/133630.
- Véron-Cetty, M-P and Philippe Véron (2010). “A catalogue of quasars and active nuclei”. In: *Astronomy and Astrophysics* 518, A10.